ChemComm

COMMUNICATION

View Article Online
View Journal | View Issue

Cite this: *Chem. Commun.*, 2021, **57**, 508

Received 25th October 2020,
Accepted 4th December 2020

DOI: 10.1039/d0cc07077g

rsc.li/chemcomm

Photocatalytic water oxidation with a Prussian blue modified brown TiO_2†

Gulsum Gundogdu, [a] T. Gamze Ulusoy Ghobadi, [b] Sina Sadigh Akbari, [a] Ekmel Ozbay [cde] and Ferdi Karadas *[ab]

A recently emerging visible light-absorbing semiconductor, brown TiO_2 (b-TiO_2), was coupled with a CoFe Prussian blue (PB) analogue to prepare an entirely earth-abundant semiconductor/water oxidation catalyst hybrid assembly. PB/b-TiO_2 exhibits a sevenfold higher photocatalytic water oxidation activity compared to b-TiO_2. An elegant band alignment unified with the optical absorption of b-TiO_2 and excellent electronic dynamics of PB yield a high-performance photocatalytic system.

TiO_2 has been the pioneer semiconductor due to its low cost, high photocatalytic activity, and photochemical stability.[1] The commercial TiO_2, however, cannot be utilized for visible light harvesting since it can only absorb and utilize ultraviolet light due to its large bandgap (3.2 eV), which accounts for a small fraction of solar light (3–5%).[2] Over the past years, considerable efforts have been made to tune the energy levels of TiO_2 and to achieve a narrow bandgap TiO_2 derivative by metal doping, nitrogen doping, and dye sensitization.[3–5] Extending the solar absorption spectrum of TiO_2 could also be achieved by creating defects that yield a black or brown color.[1] Black/brown TiO_2 derivatives have recently been investigated particularly for photocatalytic hydrogen evolution and photoelectrochemical water splitting.[6]

CoFe Prussian blue (CoFe PB) analogues have been recognized as earth-abundant and robust water oxidation catalysts (WOCs).[7–11] We have recently directed our research toward coupling them with photosensitizers and semiconductors (SCs) for efficient photocatalytic water oxidation.[12–15] Our previous studies indicate that the energy levels of the semiconductor play a critical role on the performance of PB incorporating SC-WOC assemblies. Brown TiO_2 (b-TiO_2) and CoFe PB analogues have been envisioned to have proper energy levels based on previous studies.[16–18] Herein, we prepare a CoFe PB coupled b-TiO_2 nanoparticles (PB/b-TiO_2) that is utilized for the first time for photocatalytic water oxidation. For comparison, a CoFe PB modified TiO_2 analogue (PB/TiO_2) has also been prepared by using the commercially available TiO_2, Degussa-P25.

Among the numerous synthetic routes for black/brown TiO_2, a "one-pot" gel combustion synthetic strategy[19] was employed to prepare b-TiO_2 due to its simplicity and low-cost. After rapid cooling and washing, the b-TiO_2 powder sample was obtained. For the preparation of PB/TiO_2 and PB/b-TiO_2, an *in situ* synthetic method was adopted to improve the interaction between TiO_2 and PB particles (Fig. S1, ESI,† and Fig. 1).[20]

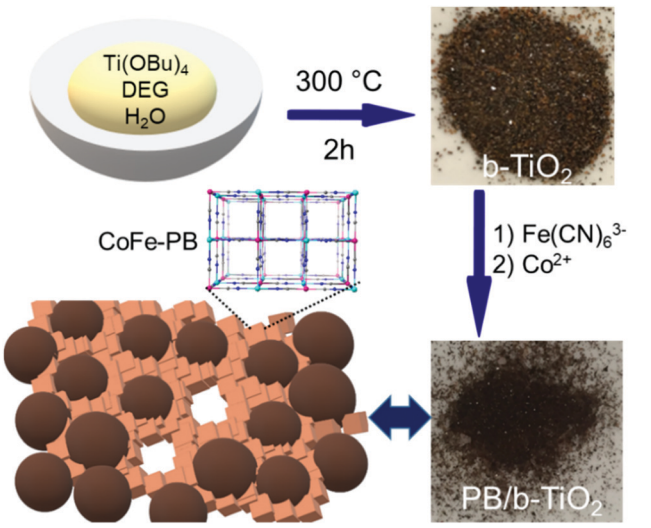

Fig. 1 The synthesis of Prussian blue incorporating brown TiO_2 assembly (PB/b-TiO_2).

[a] *Department of Chemistry, Faculty of Science, Bilkent University, Ankara 06800, Turkey. E-mail: karadas@fen.bilkent.edu.tr*
[b] *UNAM – National Nanotechnology Research Center, Institute of Materials Science and Nanotechnology, Bilkent University, Ankara 06800, Turkey*
[c] *Department of Electrical and Electronics Engineering, Bilkent University, Ankara 06800, Turkey*
[d] *NANOTAM – Nanotechnology Research Center, Bilkent University, Ankara 06800, Turkey*
[e] *Department of Physics, Bilkent University, Ankara 06800, Turkey*

† Electronic supplementary information (ESI) available. See DOI: 10.1039/d0cc07077g

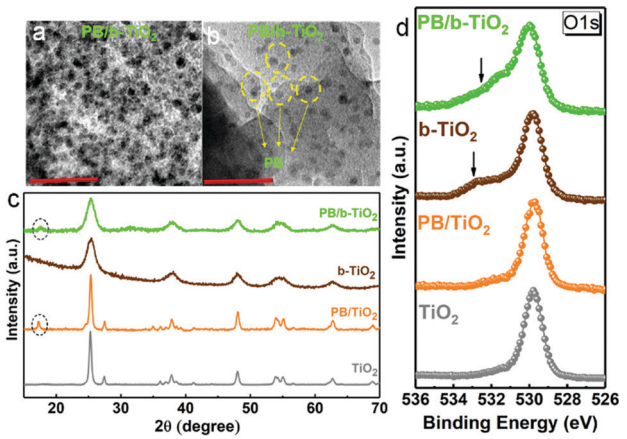

Fig. 2 HR-TEM images for (a and b) PB/b-TiO_2. Scale bars: 20 nm and 10 nm, respectively. (c) PXRD patterns for all powder samples. Dashed lines infer the PB structures. (d) The O 1s spectrum of all TiO_2 samples. The arrows show the shoulder due to oxygen vacancy formation (O_V) and/or chemisorbed oxygen species (O_C).

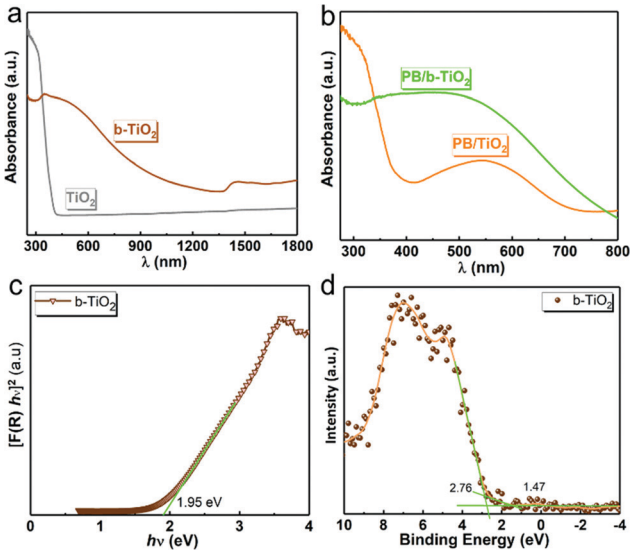

Fig. 3 UV-Vis absorption profiles for (a) TiO_2, b-TiO_2, (b) PB/TiO_2, and PB/b-TiO_2 in the 300–1800 nm wavelength range. (c) Tauc Plot used for the estimation of the optical bandgap (1.95 eV) for b-TiO_2. (d) XPS valence band spectrum of b-TiO_2. Green lines show the linear extrapolation of the curves to derive the valence band edge position of b-TiO_2, that is, $E_F - E_{VBM}$.

The SEM images for PB/TiO_2 and PB/b-TiO_2 indicate the presence of TiO_2 spherical nanoparticles with average diameters in the 24–73 nm and 25–86 nm ranges, respectively (Fig. S2–S4, ESI†). PB structures exhibit uniform distribution according to the EDS analysis (Fig. S5 and S6, ESI†). The quantitative analyses by EDS reveal a Co : Fe elemental ratio of approximately 1 : 1 for both hybrid samples while the Co : Ti atomic ratio is found to be 1 : 20 and 1 : 15, respectively, for PB/b-TiO_2 and PB/TiO_2. High-resolution transmission electron microscopy (HR-TEM) analysis suggests the formation of TiO_2 aggregates in PB/b-TiO_2 (Fig. S7, ESI†).[21] PB nanoparticles are uniformly dispersed on the surface of TiO_2 nanoparticles in PB/b-TiO_2 (Fig. 2a and b). Interplanary spacings of 0.35 nm and 0.51 nm in PB/b-TiO_2 correspond to (011) plane of the anatase phase and (200) facets of cubic PB structure, respectively (Fig. S8, ESI†).[20,22]

Powder X-ray diffraction (PXRD) patterns reveal the presence of pure anatase phase for b-TiO_2, PB/TiO_2, and PB/b-TiO_2 while TiO_2 contains a small degree of rutile phase (Fig. 2c).[23] PB/TiO_2 and PB/b-TiO_2 exhibit an additional peak at 18°, which is the characteristic feature for the cubic PB network structure.

XPS measurements are performed to elucidate the surface properties and the electronic band structures of assemblies, together with their post catalytic stabilities. An analysis of Co 2p, O 1s, and Fe 2p XPS core levels suggests the formation of a CoFe PB structure in PB/TiO_2 and PB/b-TiO_2 (Fig. 2d and Fig. S9–S11, and Tables S1, S2, ESI†).[24] Surface analysis of the b-TiO_2 using XPS revealed no Ti^{3+} signals indicating clear domination of the Ti^{4+} oxidation state (Fig. S12 and Table S3, ESI†).[19,25] O 1s region of the samples were also analyzed to understand the nature of surface defects on TiO_2. The major O 1s peak at around 530 eV is attributed to the lattice oxygen atoms (O_L) in TiO_2 as explained in our previous study (Fig. 2d).[15] This low-binding peak is attributed to O^{2-} ions connected to the Ti^{4+} ions in the bulk of TiO_2. The other component with center binding energies of around 530–532 eV is assigned to oxygen vacancy or defects (O_V) and chemisorbed oxygen species (O_C). The broad shoulders highlighted with black arrows in b-TiO_2 derivatives suggest that they have more O_V and O_C components compared to P25 ones. Furthermore, PB/b-TiO_2 has a relatively large density of O_V and O_C components. These defects in the metal oxide surface could enhance the charge separation at the surface and result in an efficient photocatalytic water splitting.[26] Beside their effect on the catalytic activity, these defect sites also improve the optical performance of the material. UV-Vis diffuse reflectance spectra (DRS) of the samples were measured to explore their absorption profiles and to elucidate their band energy alignments (Fig. 3a and b). As shown in Fig. 3a, the Degussa-P25 exhibits a strong absorption at a wavelength shorter than 390 nm in the UV region, while b-TiO_2 has an absorption tail extended through the visible region. For PB/TiO_2, a new broad absorption band is observed in the 415–715 nm visible region due to metal-to-metal charge transfer in the CoFe PB structure. The absorption of PB/b-TiO_2 is enhanced and shifted by around 100 nm further in the visible region compared to bare b-TiO_2. This data is also used to examine the band gap of Degussa-P25 and b-TiO_2, respectively (see Fig. 3c and Fig. S13, ESI†). The absorption data were fitted according to $(F(R_\infty)\ h\nu)^n$ for both direct and indirect allowed bandgap transitions.[27] The choice of direct or indirect transition for both samples are explained in the ESI,† section and shown in Fig. S13.

The energetic level of the valence band maximum (VBM) (*i.e.* $E_F - E_{VBM}$, where the Fermi level energy (E_F) is the zero point) for commercial TiO_2 and b-TiO_2 can be estimated by a combination of optical data and XPS measurement of the VB spectra. As displayed in Fig. 3d, the dominant response arose from the bulk TiO_2, $E_{VBM} - E_F$, is found to be 2.76 eV with a tail corresponding to 1.47 eV for b-TiO_2. A difference of 1.29 eV, which is observed from VB XPS, strongly suggests the presence of the defect states in b-TiO_2. b-TiO_2, thus, has a narrower bandgap (1.95 eV) due to band tailing. XPS analysis also

suggests that these surface defects are originated mainly from oxygen vacancies rather than potential Ti^{3+} sites.

An indicator for the oxygen vacancy degree is the VBM value, which is correlated well with the increase in the oxygen vacancy degree.[16] Given the slight shift of the VBM in b-TiO_2 (1.47 eV) compared to that in a previously reported black TiO_2 (1.52 eV),[19] the origin of brown color could, thus, be attributed to the decrease in the oxygen vacancies with respect to black TiO_2 (Fig. 3d). The binding energy difference, $\Delta BE = BE(O\ 1s) - BE(Ti\ 2p_{3/2})$, is found to be equal to 71.2 eV for TiO_2 and b-TiO_2, 71.3 eV for PB/TiO_2, and 71.4 eV for PB/b-TiO_2, which are comparable to that of the anatase phase ($\sim$71.4 eV), which verifies the domination of the Ti^{4+} state in the compounds.[28] The absence of Ti^{3+} peaks indicates that Ti^{3+} contamination is well below $\sim$1 and 2%.[25,29] In a previous work,[13] we deduced the oxidation level of CoFe PB to be 0.06 eV lower than the water oxidation process (0.83 eV at pH 7). Since metal oxides exhibit dominant VB responses compared to CoFe PB, these energetic locations were also used for PB/TiO_2 and PB/b-TiO_2. Given the results mentioned hereinabove, the overall band alignments for PB/TiO_2 and PB/b-TiO_2 are established in Fig. 4.[30] According to the band energy diagram, a proper alignment is achieved between the VB of b-TiO_2 and the energy level of CoFe PB. The photocatalytic process is initiated with the absorption of light by white and brown TiO_2, which generates electrons and holes. The holes in the VB of TiO_2 are transferred to the HOMO level CoFe PB, which is positioned in between the VB of TiO_2 and the water oxidation level. These holes are then utilized for the water oxidation process. On the other hand, the electrons in the conduction band of TiO_2 are consumed by the electron scavenger, $S_2O_8^{2-}$.

The oxygen evolution activity of b-TiO_2 (4.8 μmol h^{-1}) is around two times higher than that of bare TiO_2 (2.4 μmol h^{-1}) as expected. The activities of both TiO_2 samples are significantly enhanced when they are coated with PB structures (Fig. 5). A remarkable activity of approx. 35.6 μmol h^{-1} is obtained for PB/b-TiO_2, which is around 5.5 times higher than that obtained for PB/TiO_2 (6.5 μmol h^{-1}). The broadening of the VB of TiO_2 has a twofold effect in the photocatalytic activity: (i) the number of photons absorbed by SC is enhanced, which results in an activity difference between TiO_2 and b-TiO_2, (ii) the close proximity between VB of b-TiO_2 and HOMO energy level of PB in PB/b-TiO_2 provides a fast interfacial electron dynamic in PB/TiO_2. For this reason, a trend as follows is obtained; PB/b-TiO_2 > PB/TiO_2 > b-TiO_2 > TiO_2. Photocatalytic activities of several TiO_2 incorporating assemblies are summarized in Table S4 (ESI†). Although each study has been performed under different conditions, the comparison of our results with previous studies indicates that the coupling of TiO_2 with PB structures is a simple and effective method to develop photocatalytic suspensions for efficient water oxidation from ultraviolet towards the visible region. The photocatalytic activity of PB/b-TiO_2 is retained for five consecutive cycles, a total of 10 h. XPS measurements are performed on pristine and post-catalytic samples to evaluate the stability of hybrid assemblies. O 1s, Fe 2p, and Co 2p regions of pristine and post-catalytic samples exhibit similar profiles

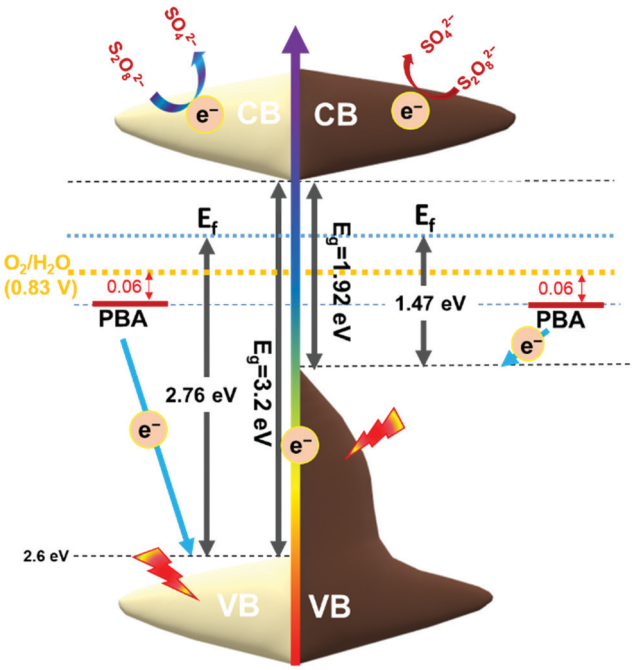

Fig. 4 Energy band diagram of PB/TiO_2 and PB/b-TiO_2 for the water oxidation process involving the electron transfer mechanism.

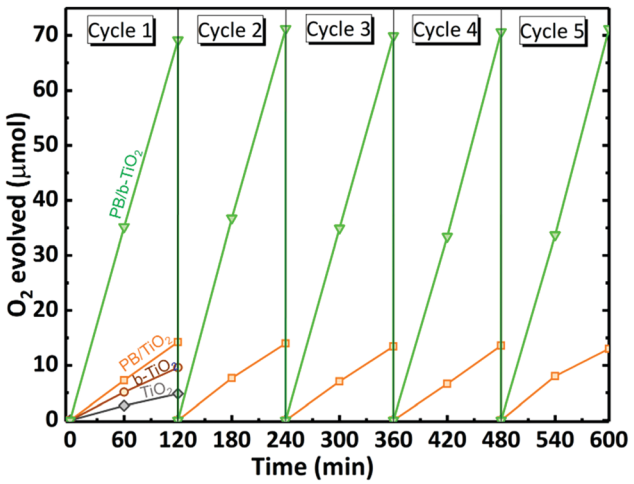

Fig. 5 Photocatalytic oxygen evolution profiles by TiO_2, b-TiO_2, PB/TiO_2, and PB/b-TiO_2 (27 mg for each) and $Na_2S_2O_8$ (27 mg) in pH 7, 0.1 M phosphate buffer solution batch was used in each cycle.

(Fig. S9–S11, ESI†). Furthermore, the sharp cyanide stretches of PB structure are observed at 2115 and 2122 cm^{-1} (Fig. S14, ESI†), respectively for PB/b-TiO_2 and PB/TiO_2, which are observed also for the post-catalytic samples (Fig. S15, ESI†).[31] Thus, XPS and Infrared studies performed on the post-catalytic samples confirm the stabilities of the hybrid samples under photocatalytic conditions.

Photoluminescence (PL) spectroscopy has been widely used to investigate the separation, transfer, and recombination of the photogenerated electron–hole pairs.[32,33] The PL intensity

and its spectral bandwidth are defined by the radiative decay mechanisms in the semiconductor including the direct band-to-band transition and shallow-deep trap states. A decrease in the PL intensity is expected when the semiconductor is supported with a charge extraction layer such as the PB structure that provides selective charge separation. Fig. S16 (ESI†) reveals a remarkable decrease in the PL intensity of the hybrid samples (PB/TiO_2 and $PB/b\text{-}TiO_2$) compared to pristine TiO_2 and $b\text{-}TiO_2$, which indicate an enhanced charge separation in the hybrid samples. This result is in good agreement with previous studies, which utilize a CoFe PB layer as a catalyst on TiO_2 and $BiVO_4$ modified photoelectrodes to decrease the recombination of photogenerated electrons and holes for enhanced photocatalytic performance.[13–15,34,35]

Further insight on carrier dynamics can also be acquired by evaluating the PL spectra of bare samples. As shown in Fig. S16 (ESI†), the emission peaks were observed for TiO_2 and PB/TiO_2 at 362 nm and 378 nm. The PL emission spectra of $b\text{-}TiO_2$ and $PB/b\text{-}TiO_2$ samples exhibit a peak at 362 nm as well as a broad distribution up to 500 nm wavelength (Fig. S16, ESI†). The response in longer wavelengths originates from the defects within the bandgap of $b\text{-}TiO_2$. This is in line with XPS results, which suggest the formation of oxygen defects in $b\text{-}TiO_2$.[36]

The photocatalytic water oxidation performance of $PB/b\text{-}TiO_2$ depends on many factors such as the molar ratio of PB, the defect concentration, defect energetic location, valence band (VB), and conduction band (CB) levels. $PB2/b\text{-}TiO_2$ with a 1 : 10 ($PB:TiO_2$) molar ratio was also prepared to see the effect of molar ratio of PB on the photocatalytic water oxidation performance (see EDS, Fig. S17, ESI†). $PB2/b\text{-}TiO_2$ exhibits a lower activity with *ca.* 26 μmol h^{-1} compared to $PB/b\text{-}TiO_2$ (*ca.* 35.6 μmol h^{-1}, 1 : 20 $PB:TiO_2$ ratio), probably due to the aggregation of excess PB particles during the photocatalytic process and/or relatively low physical surface interaction between PB and TiO_2 particles.[37] Another reason could be the parasitic light absorption by PB assembly ($415\ nm < \lambda < 715\ nm$) that reduces the amount of light absorbed by the semiconductor host.

In conclusion, $PB/b\text{-}TiO_2$ exhibits a remarkable photocatalytic oxidation activity compared to $b\text{-}TiO_2$ and PB/TiO_2, which is attributed to the proper band energy alignment and efficient absorption of $b\text{-}TiO_2$ in the visible region. The hybrid assembly maintains its stability throughout a 10 h photocatalytic water oxidation process. The simplicity of the approach paves the way for scalable and earth-abundant photocatalytic SC-WOC systems.

Conflicts of interest

There are no conflicts to declare.

Notes and references

1 X. Yan, Y. Li and T. Xia, *Int. J. Photoenergy*, 2017, 8529851.
2 X. Chen and C. Burda, *J. Am. Chem. Soc.*, 2008, **130**, 5018–5019.
3 J. Schneider, M. Matsuoka, M. Takeuchi, J. Zhang, Y. Horiuchi, M. Anpo and D. W. Bahnemann, *Chem. Rev.*, 2014, **114**, 9919–9986.
4 C. Chen, W. Ma and J. Zhao, *Chem. Soc. Rev.*, 2010, **39**, 4206–4219.
5 D. Ma, A. Liu, S. Li, C. Lu and C. Chen, *Catal. Sci. Technol.*, 2018, **8**, 2030–2045.
6 B. Wang, S. Shen and S. S. Mao, *J. Materiomics*, 2017, **3**, 96–111.
7 F. S. Hegner, I. Herraiz-Cardona, D. Cardenas-Morcoso, N. López, J. R. Galán-Mascarós and S. Gimenez, *ACS Appl. Mater. Interfaces*, 2017, **9**, 37671–37681.
8 E. P. Alsaç, E. Ülker, S. V. K. Nune, Y. Dede and F. Karadas, *Chem. – Eur. J.*, 2018, **24**, 4856–4863.
9 Y. Yamada, K. Oyama, R. Gates and S. Fukuzumi, *Angew. Chem., Int. Ed.*, 2015, **54**, 5613–5617.
10 B. M. Pires, P. L. Dos Santos, V. Katic, S. Strohauer, R. Landers, A. L. B. Formiga and J. A. Bonacin, *Dalton Trans.*, 2019, **48**, 4811–4822.
11 S. Pintado, S. Goberna-Ferrón, E. C. Escudero-Adán and J. R. Galán-Mascarós, *J. Am. Chem. Soc.*, 2013, **135**, 13270–13273.
12 Z. Kap and F. Karadas, *Faraday Discuss.*, 2019, **215**, 111–122.
13 T. G. Ulusoy Ghobadi, A. Ghobadi, M. Buyuktemiz, E. A. Yildiz, D. Berna Yildiz, H. G. Yaglioglu, Y. Dede, E. Ozbay and F. Karadas, *Angew. Chem., Int. Ed.*, 2020, **59**, 4082–4090.
14 T. G. Ulusoy Ghobadi, E. Akhuseyin Yildiz, M. Buyuktemiz, S. Sadigh Akbari, D. Topkaya, Ü. İsci, Y. Dede, H. G. Yaglioglu and F. Karadas, *Angew. Chem.*, 2018, **130**, 17419–17423.
15 T. G. U. Ghobadi, A. Ghobadi, M. C. Soydan, M. B. Vishlaghi, S. Kaya, F. Karadas and E. Ozbay, *ChemSusChem*, 2020, **13**, 2483.
16 S. G. Ullattil and P. Periyat, *Nanoscale*, 2015, **7**, 19184–19192.
17 X. Chen, L. Liu and F. Huang, *Chem. Soc. Rev.*, 2015, **44**, 1861–1885.
18 X. Chen, L. Liu, P. Y. Yu and S. S. Mao, *Science*, 2011, **331**, 746–750.
19 S. G. Ullattil and P. Periyat, *J. Mater. Chem. A*, 2016, **4**, 5854–5858.
20 X. Li, J. Wang, A. I. Rykov, V. K. Sharma, H. Wei, C. Jin, X. Liu, M. Li, S. Yu, C. Sun and D. D. Dionysiou, *Catal. Sci. Technol.*, 2015, **5**, 504–514.
21 K. Szaciłowski, W. Macyk and G. Stochel, *J. Mater. Chem.*, 2006, **16**, 4603–4611.
22 L. Ren, J. G. Wang, H. Liu, M. Shao and B. Wei, *Electrochim. Acta*, 2019, **321**, 134671.
23 W. Saeed, A.-B. Al-Odayni, A. Alghamdi, A. Alrahlah and T. Aouak, *Crystals*, 2018, **8**, 452.
24 R. O. Lezna, R. Romagnoli, N. R. D. Tacconi and K. Rajeshwar, *J. Phys. Chem. B*, 2002, **106**, 3612–3621.
25 V. V. Atuchin, *J. Mater. Chem. A*, 2017, **5**, 426–427.
26 A. Naldoni, M. Altomare, G. Zoppellaro, N. Liu, Š. Kment, R. Zbořil and P. Schmuki, *ACS Catal.*, 2019, **9**, 345–364.
27 P. Makuła, M. Pacia and W. Macyk, *J. Phys. Chem. Lett.*, 2018, **9**, 6814–6817.
28 V. V. Atuchin, V. G. Kesler, N. V. Pervukhina and Z. Zhang, *J. Electron Spectrosc. Relat. Phenom.*, 2006, **152**, 18–24.
29 X. Wang, R. Fu, Q. Yin, H. Wu, X. Guo, R. Xu and Q. Zhong, *J. Nanopart. Res.*, 2018, **20**, 1–10.
30 M. Bledowski, L. Wang, A. Ramakrishnan, O. V. Khavryuchenko, V. D. Khavryuchenko, P. C. Ricci, J. Strunk, T. Cremer, C. Kolbeck and R. Beranek, *Phys. Chem. Chem. Phys.*, 2011, **13**, 21511–21519.
31 M. Berrettoni, M. Giorgetti, S. Zamponi, P. Conti, D. Ranganathan, A. Zanotto, M. L. Saladino and E. Caponetti, *J. Phys. Chem. C*, 2010, **114**, 6401–6407.
32 F. B. Li and X. Z. Li, *Chemosphere*, 2002, **48**, 1103–1111.
33 K. Parida, M. Satpathy and L. Mohapatra, *J. Mater. Chem.*, 2012, **22**, 7350–7357.
34 B. Moss, F. S. Hegner, S. Corby, S. Selim, L. Francàs, N. López, S. Giménez, J. R. Galán-Mascarós and J. R. Durrant, *ACS Energy Lett.*, 2019, **4**, 337–342.
35 B. M. Pires, F. S. Hegner, J. A. Bonacin and J. R. Galán-Mascarós, *ACS Appl. Energy Mater.*, 2020, **3**, 8448–8456.
36 L. Li, K. Shi, R. Tu, Q. Qian, D. Li, Z. Yang and X. Lu, *Chin. J. Catal.*, 2015, **36**, 1943–1948.
37 M. Giorgetti, G. Aquilanti, M. Ciabocco and M. Berrettoni, *Phys. Chem. Chem. Phys.*, 2015, **17**, 22519–22522.